

000 001 002 003 004 005 006 007 008 009 DESIGN OF LIGAND-BINDING PROTEINS WITH ATOMIC FLOW MATCHING

005 **Anonymous authors**

006 Paper under double-blind review

ABSTRACT

010 Designing novel proteins that bind to small molecules is a long-standing challenge
 011 in computational biology, with applications in developing catalysts, biosensors,
 012 and more. Current computational methods rely on the assumption that the binding
 013 pose of the target molecule is known, which is not always feasible, as conforma-
 014 tions of novel targets are often unknown and tend to change upon binding. In
 015 this work, we formulate proteins and molecules as unified biotokens, and present
 016 ATOMFLOW, a novel deep generative model under the flow-matching framework
 017 for the design of ligand-binding proteins from the 2D target molecular graph alone.
 018 Operating on the positions of biotokens, ATOMFLOW captures the flexibility of
 019 ligands and generates ligand conformations and protein backbone structures it-
 020 eratively. We consider the multi-scale nature of biotokens and demonstrate that
 021 ATOMFLOW can be effectively trained on a subset of structures from the Protein
 022 Data Bank, by matching the flow vector field using an $SE(3)$ equivariant structure
 023 prediction network. Experimental results demonstrate that our method generates
 024 high-fidelity ligand-binding proteins, matching or surpassing the performance of
 025 RFDiffusionAA across multiple metrics—without requiring bound ligand struc-
 026 tures. As a general framework, ATOMFLOW can be readily extended to diverse
 027 biomolecule design tasks in the future.

028 1 INTRODUCTION

030 Proteins are indispensable macromolecules that drive the essential processes of living organisms. A
 031 crucial mechanism by which they accomplish this is through binding with small molecules (Schreier
 032 et al., 2009). Continuous progress has been made to design ligand-binding proteins with various
 033 biological functions, such as catalysts and biosensors (Bennett et al., 2023). However, the problem
 034 remains challenging due to the complex interactions between proteins and molecules, as well as the
 035 inherent flexibility of ligands. The most well-established approaches depend on shape complementar-
 036 ity to dock molecules onto native protein scaffold structures (Bick et al., 2017; Polizzi & DeGrado,
 037 2020), which are computationally expensive.

038 RFDiffusionAA (Krishna et al., 2024) is cur-
 039 rently the leading model for *de novo* pro-
 040 tein design targeting small molecule ligands.
 041 Based on the all-atom structure prediction
 042 model RoseTTAFoldAA (Krishna et al., 2024),
 043 it achieves strong performance in generating
 044 ligand-binding proteins and improves upon its
 045 predecessor RFDiffusion (Watson et al., 2023),
 046 which does not directly model protein-ligand
 047 interaction. A key limitation of RFDiffusionAA
 048 is its assumption that the ligand adopts a known
 049 and rigid binding conformation. This assump-
 050 tion does not hold for many ligands, especially
 051 those without known binding poses (Bick et al., 2017). Although diverse conformers can be sampled
 052 and filtered using expert heuristics (Krishna et al., 2024), this process is computationally intensive.
 053 In addition, ligands often exhibit conformational flexibility upon binding (Mobley & Dill, 2009), as
 shown in Figure 1. Recently, AlphaFold 3-like models have shown the ability to capture ligand flexi-
 bility during docking (Abramson et al., 2024). While they can be repurposed for binder design (Yang

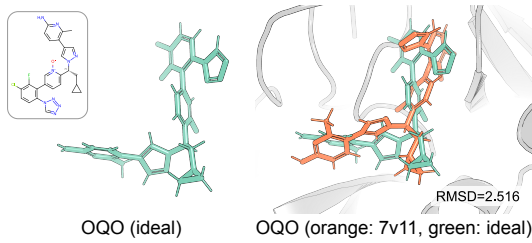


Figure 1: The conformer of OQO deforms upon binding to coagulation factor XIa. Green: ideal conformer. Orange: bound conformer.

et al.), achieving practical performance has so far required large-scale post-training, and existing work remains limited to CDR loop design and constrained by the fixed model architecture.

	ATOMFLOW	RFDiffusionAA	RFDiffusion	AlphaFold 3
De novo Design Capability	✓	✓	✓	✓ with repurposing
Contact-Based Modeling	✓	✓	✗	✓
Ligand Flexibility	✓	✗	✗	✓
Pretrained Model Independence	✓	✗	✗	✗

Table 1: Comparison of key features across the methods.

To address the aforementioned issues, we present Atomic Flow-matching (ATOMFLOW), a novel deep generative model with a flow-matching framework (Lipman et al., 2022; Liu et al., 2022) on atomic biotokens for the design of ligand-binding proteins from 2D molecular graphs alone. Key features of ATOMFLOW are compared in Table 1. We model different types of biomolecules within a unified framework that operates in a shared spatial representation, which maximizes information aggregation (Bryant et al., 2024), with a flow matching model that directly designs the interactions. Instead of relying on a fixed ligand conformer, ATOMFLOW learns to update the ligand structure along with the structure of the protein binder. We define a flow on the representative atoms of the tokens as a linear interpolation between the bound protein-ligand complex structures and noisy structures and demonstrate that, with minor approximations, the vector field of the defined flow can be effectively learned using an SE(3)-equivariant structure module and a variant of Frame Aligned Point Error (FAPE) loss (Jumper et al., 2021) that compensates for the multi-scale nature of their geometric features.¹ The concept of regressing the vector field through structure denoising has also been explored in Jing et al. (2024), though their work focuses on conformer prediction and depends on a pre-trained structure prediction model.

We designed an *in silico* evaluation pipeline for this task, evaluating ATOMFLOW on multiple metrics following previous works (Krishna et al., 2024). We also introduce an alternative binding affinity metric based on the confidence scores of AlphaFold 3-like models (Abramson et al., 2024; team et al., 2024), which is experimentally validated to correlate strongly with binding potential in minibinder design (Zambaldi et al., 2024). The performance of ATOMFLOW outperforms or is comparable to RFDiffusionAA, with flexible ligand conformer modeling and more than 5x faster inference speed. A case study further highlights that when the bound structure is unknown, ATOMFLOW successfully designs protein binders with more interatomic contacts, whereas RFDiffusionAA can be constrained by its dependence on a fixed, suboptimal ligand structure.

2 RELATED WORK

Ligand-binding Protein Design. Traditional approaches to ligand-binding protein design mainly rely on docking molecules onto large sets of shape-complementary protein pockets (Polizzi & DeGrado, 2020; Lu et al., 2024). While the screening process can be accelerated with deep learning models (An et al., 2023), conventional methods are computationally expensive and often depend on domain experts (Bick et al., 2017). Recent advances in deep generative models have paved the way for data-driven approaches, and a variety of models have been proposed to design proteins conditioned on binding targets (Shi et al., 2022; Kong et al., 2023; Watson et al., 2023; Zhang et al., 2024). Focusing on molecule binder design, RFDiffusion (Watson et al., 2023) generates novel proteins from scratch, using a heuristic attractive-repulsive potential to measure shape complementarity. The follow-up work RFDiffusionAA (Krishna et al., 2024) improves the performance by explicitly modeling the interactions between proteins and molecules with an all-atom formulation. These approaches assume binding poses of ligands are known and impose rigidity constraints on ligand structures. Another line of research focuses on designing binding pockets for small molecules (Stark et al., 2024; Zhang et al., 2024). While taking ligand flexibility into consideration, they can only design the portions of proteins that interact with the ligands and require the rest part of the proteins as input. Our model also accounts for the ligand flexibility, but is able to design full ligand-binding proteins from 2D molecular graph alone.

Protein Generative Model and Structure Prediction. Recently, various deep generative models for protein generation have emerged (Ingraham et al., 2023; Lin & AlQuraishi, 2023; Yim et al.,

¹The size of a protein is often much larger than that of a molecule. The size disparity should be considered when designing flow-matching models for stable training and inference.

2023b;a; Wu et al., 2024; Watson et al., 2023; Krishna et al., 2024). For example, Genie (Lin & AlQuraishi, 2023) introduces a diffusion process defined on $C\alpha$ coordinates of proteins and allows for the incorporation of motif structures as conditions. FrameDiff (Yim et al., 2023b) takes a step further by generating novel protein backbone structures using an $SE(3)$ diffusion process applied to residue frames. Its successor, FrameFlow (Yim et al., 2023a), accelerates the generation process by leveraging the flow-matching framework. However, these approaches are tailored for single-chain protein generation and fall short in modeling multiple biomolecules. Recent development of all-atom strucutre prediction models such as RoseTTAFoldAA (Krishna et al., 2024) and AlphaFold 3 (Abramson et al., 2024) tokenize various types of biomolecules into unified tokens, aiming to develop a universal structure prediction model for all molecular types presented in the Protein Data Bank. Emerging work has explored repurposing structure prediction models like AlphaFold 3 as generators, though current efforts are limited to antibody CDR design rather than complete protein generation (Yang et al.). RFDiffusion 2 generates protein binders based on fixed fragmented pocket residues without the need to specify their sequential locations (Ahern et al., 2025). Our method adopts a similar formulation, leveraging unified tokenization to enhance information exchange between proteins and other biomolecules (Bryant et al., 2024).

3 PRELIMINARIES

3.1 NOTATIONS AND PROBLEM FORMULATION

Notations. In this work, a protein-ligand complex is represented as a series of N biotokens $\{a_i \mid a_i = (s_i, x_i), i = 1, 2, \dots, N\}$, where each token a_i corresponds to either a protein residue or a ligand atom, s_i denotes the token type, and $x_i \in \mathbb{R}^3$ denotes the token position, i.e. the coordinate of its representative atom. Let $\mathcal{S}_{\text{protein}}$ and $\mathcal{S}_{\text{atom}}$ be the set of amino acid types and chemical elements, respectively. For protein residues, $s_i \in \mathcal{S}_{\text{protein}}$, with x_i being the position of the $C\text{-}\alpha$ carbon. For ligand atoms, $s_i \in \mathcal{S}_{\text{atom}}$, with x_i being the atomic position. We define the protein token set as $\mathcal{P} = \{a_i \mid s_i \in \mathcal{S}_{\text{protein}}\}$, with $N_p = |\mathcal{P}|$ being the number of protein residues, and the ligand token set as $\mathcal{M} = \{a_i \mid s_i \in \mathcal{S}_{\text{atom}}\}$, with $N_m = |\mathcal{M}|$ representing the number of ligand atoms. In our settings, $N = N_p + N_m$. The biotokens are attributed with token-level features $f^{\text{token}} \in \mathbb{R}^{N \times c_t}$ and pair-level features $f^{\text{pair}} \in \mathbb{R}^{N \times N \times c_p}$, where c_t and c_p denote the feature dimensions.

Problem Formulation. Given a ligand molecule represented as a chemical graph $\mathcal{G} = (\mathcal{V}, \mathcal{E})$ and a residue count N_p for the protein binder to be designed, we aim to generate a protein-ligand complex, where a conformer of \mathcal{G} is docked to a protein binder with N_p residues. Specifically, by describing the target protein-ligand complex as a series of biotokens, we generate the token positions $\{x_i\}$, with $\mathbf{x}_m = \{x_i \mid a_i \in \mathcal{M}\}$ being a valid conformer for \mathcal{G} , and $\mathbf{x}_p = \{x_i \mid a_i \in \mathcal{P}\}$ being a protein binder with high binding affinity to \mathbf{x}_m . Following previous works (Krishna et al., 2024; Yim et al., 2023b), we additionally generate the token frames $\{T_i = (r_i, t_i) \mid a_i \in \mathcal{P}\}$ for protein tokens as described in Appendix A.1, which can be used to recover full backbone coordinates of residues. The design of residue types $\{s_i \mid a_i \in \mathcal{P}\}$ is delegated to an existing reverse folding model (Dauparas et al., 2023).

3.2 FLOW MATCHING

Building upon the significant success of diffusion models in various generative tasks, flow matching models (Albergo & Vanden-Eijnden, 2022; Liu et al., 2022) allow for faster and more reliable sampling from a distribution learned from data. The generative process of flow matching models is usually defined by a probability path $p_t(x)$, $t \in [0, 1]$ that gradually transforms from a known noisy distribution $p_0(x) = q(x)$, such as $\mathcal{N}(x|0, I)$ for $x \in \mathbb{R}$, to an approximate data distribution $p_1 \approx p_{\text{data}}(x)$. A vector field $u_t(x)$, which leads to an [ordinary differential equation \(ODE\)](#) $\frac{d\phi_t(\mathbf{x})}{dt} = u_t(\phi_t(\mathbf{x}))$, is used to generate the probability path via the push-forward equation,

$$p_t = [\phi_t]_* p_0 = p_0(\phi_t^{-1}(x)) \det \left[\frac{\partial \phi_t^{-1}}{\partial x}(x) \right], \quad (1)$$

which could be approximated with a trainable network $\hat{v}_t(x; \theta)$.

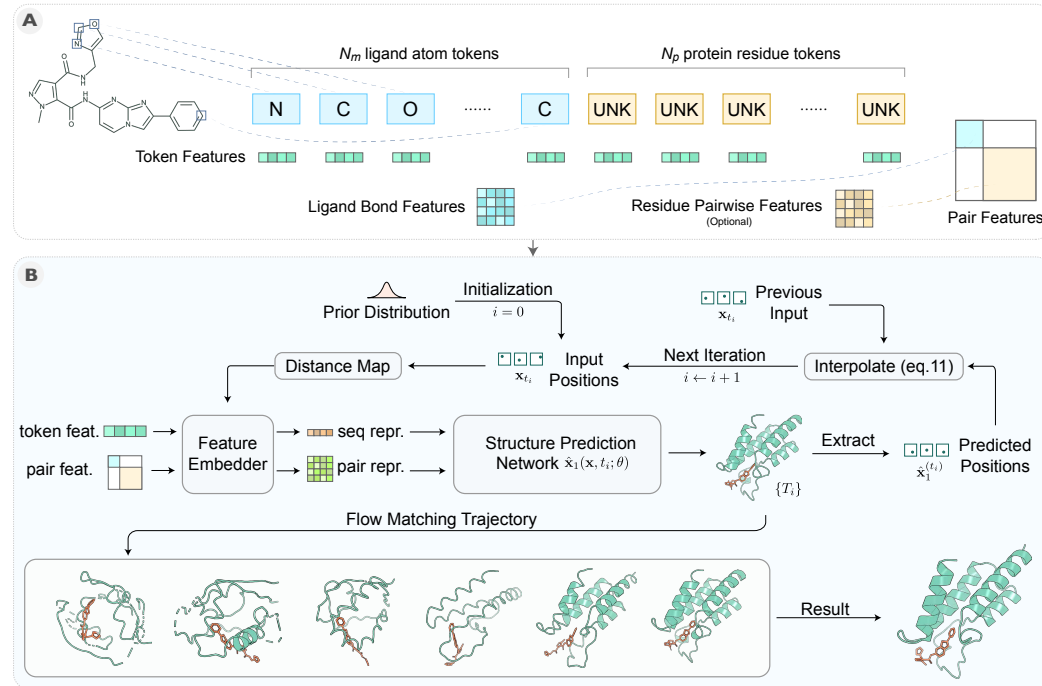
Due to the complexity of defining an appropriate p_t and u_t , we could alternatively define a conditional probability path $p_t(x|x_1)$, which is usually derived through a conditional vector field $u_t(x|x_1)$ for each data point x_1 (Lipman et al., 2022). The conditional vector field is then approximated with a trainable network $\hat{v}_t(x; \theta)$. The conditional flow matching loss,

$$\mathcal{L}_{\text{CFM}}(\theta) = \mathbb{E}_{t, p_{\text{data}}(x_1), p_t(x|x_1)} \|\hat{v}_t(x; \theta) - u_t(x|x_1)\|, \quad (2)$$

162 is proved to have identical gradients w.r.t. θ with $\mathcal{L}_{\text{FM}} = \mathbb{E}_{t, p_{\text{data}}(x)} \|\hat{v}_t(x; \theta) - u_t(x)\|$ (Lipman et al., 2022), which means the model can generate a marginal vector field by simply learning from the x_1 -conditioned vector fields, without access to $p_t(x)$ and $u_t(x)$. After training, a neural ODE is obtained, ready for sampling from p_0 to p_t with an ODE solver (Jardine, 2011).

4 METHOD

168 ATOMFLOW uses a unified *biotoken* representation to jointly generate protein and ligand structures
169 by learning the distribution of token positions conditioned on a ligand chemical graph \mathcal{G} . Figure 2
170 illustrates the overall framework. We introduce a rectified flow on token positions $\mathbf{x} \in \mathbb{R}^{N \times 3}$ and
171 approximate its vector field with an $\text{SE}(3)$ -equivariant structure prediction network. In this section,
172 we introduce the flow matching model in Section 4.1, the biotoken feature representation in Section
173 4.2, the structure prediction module in Section 4.3, and the training and inference procedures in
174 Section 4.4. The overview of our method is illustrated in Figure 2.



198 Figure 2: The inference process of ATOMFLOW. We represent the protein-ligand complex as a series
199 of biotokens and embed their token and pair-level features (residue pairwise features are optional, see
200 Appendix A.2). Starting from a noisy sample, the flow matching procedure gradually generates the
201 designed structure x_1 with a structure prediction network.

4.1 FLOW MATCHING FOR PROTEIN-LIGAND COMPLEX GENERATION

204 For all types of tokens, we only consider their token positions to simplify the flow matching process.
205 Thus, the positions of all tokens lie in the Euclidean space $\mathbb{R}^{N \times 3}$. Since a complex could be arbitrarily
206 moved or rotated without changing its structure, we need to treat different coordinate representations
207 as the same if they could be aligned with an $\text{SE}(3)$ translation. Thus, every sample lies in the quotient
208 space $Q : \mathbb{R}^{N \times 3} / \text{SE}(3)$. We define a rectified flow on Q using a conditional vector field

$$209 \quad u_t(\mathbf{x} | \mathbf{x}_1) = \frac{1}{1-t} \left(\text{align}_{\mathbf{x}}(\mathbf{x}_1) - \mathbf{x} \right), \quad (3)$$

211 where \mathbf{x}_1 is the target structure from the data distribution, and $\text{align}_{\mathbf{x}}(\mathbf{x}_1)$ is its best root mean
212 square deviation (RMSD) alignment to \mathbf{x} . We train the network to approximate $u_t(\mathbf{x} | \mathbf{x}_1)$ by
213 minimizing $\mathcal{L}_{\text{CFM}}(\theta)$. With approximation (Appendix A.3), we find it more numerically stable to
214 use an FAPE-based loss (Jumper et al., 2021), which does not change the final training target.

$$215 \quad \mathcal{L}_{\text{CFM-FAPE}}(\theta) = \mathbb{E}_{t, p_{\text{data}}(\mathbf{x}_1), p_t(\mathbf{x} | \mathbf{x}_1)} \left[\frac{1}{1-t} \text{FAPE}(\hat{\mathbf{x}}_1(\mathbf{x}, t; \theta), \mathbf{x}_1) \right]. \quad (4)$$

216 Here, $\hat{\mathbf{x}}_1$ is predicted by our structure network. We partition the FAPE loss into protein-protein,
 217 protein-ligand, and ligand-ligand interactions with appropriate scaling factors.
 218

219 4.2 REPRESENTATION OF CONDITIONAL FEATURES

220 The generation process of ATOMFLOW is conditioned on the ligand chemical graph \mathcal{G} and a designated
 221 protein length N_p . We model such conditions as an additional condition to the vector field u . As a
 222 result, the inputs of the prediction network $\hat{\mathbf{x}}_1$ are augmented to accept conditional features. With the
 223 biotoken representation, we embed all such features as f^{token} and f^{pair} as illustrated in Figure 2A.
 224

225 For a ligand chemical graph \mathcal{G} , we embed the chemical properties as f^{token} of ligand tokens. The
 226 chemical bonds \mathcal{E} are embedded in f^{pair} as a multi-dimensional adjacency tensor, each dimension
 227 representing a bond type. For residue tokens, we embed the relative residue position (Shaw et al.,
 228 2018) in f^{pair} , while f^{token} may represent other known conditions. We concatenate the protein and
 229 ligand features to form a unified feature tensor, eliminating the need to distinguish different types of
 230 tokens when processing the features. Further details are provided in Appendix A.2.
 231

232 4.3 STRUCTURE PREDICTION NETWORK

233 The structure prediction network $\hat{\mathbf{x}}_1(\mathbf{x}, t; \theta)$ ² predicts the token frames $\{T_i\}$, which can be used
 234 to extract token positions \mathbf{x}_1 , given a series of noisy positions \mathbf{x} at timestamp t . It encodes \mathbf{x} ,
 235 along with f^{token} and f^{pair} , with an SE(3) invariant encoding module, processing the representation
 236 with a transformer stack, and generates the predicted structure with a structure module based on
 237 invariant-point attention (IPA) (Jumper et al., 2021), as illustrated in Figure 2B. The network jointly
 238 processes two kinds of biotokens, protein residues and ligand atoms, with different spatial scales, and
 239 handles such differences with special care.
 240

241 Distance Map. The input coordinates \mathbf{x} are encoded by projecting the one-hot binned distance map
 242 between input coordinates for each token pair to the feature space

$$243 t_{i,j} = \text{Linear}(\text{BinRepr}(\|\mathbf{x}^{(i)} - \mathbf{x}^{(j)}\|)), \quad (5)$$

244 where the bins are not divided equally considering the different precision requirements between
 245 residues and atoms. This representation is SE(3) invariant, since the internal distance does not change
 246 under rigid transformation.³

247 **248 Feature Embedder.** The feature embedder generates a single representation $s \in \mathbb{R}^{N \times c_s}$ and pair
 249 representation $z \in \mathbb{R}^{N \times N \times c_z}$ from distance map h , noise level t , f^{token} and f^{pair} for the following
 250 steps. The noise level is encoded with Gaussian Fourier embedding (Song et al., 2021). The
 251 local features are concatenated and projected to single representation s and pair representation z ,
 252 $s_i = \text{Linear}(f_i^{\text{local}})$. The pair features and input encoding are projected and added to z

$$253 z_{i,j} = \text{Linear}(f_i^{\text{local}}) + \text{Linear}(f_j^{\text{local}}) + f_{i,j}^{\text{pair}} + t_{i,j}. \quad (6)$$

254 As described in Section 4.2, different token types can be treated the same and processed uniformly.
 255

256 **257 Structure Module.** The structure module generates a predicted complex structure, represented as a
 258 series of token frames T^N . For ligand atoms, the rotation of the predicted frame is always identity
 259 rotation, while the translation equals its position. It first processes z through a deep transformer stack
 260 (Appendix A.4) to obtain a denoised pair representation z' , and converts s and z' to T^N through a
 261 series of shared-weight IPA block

$$262 T_{1\dots N} = \text{IPASStack}(s_{1\dots N}, \text{TransformerStack}(z_{1\dots N, 1\dots N})). \quad (7)$$

263 The IPA stack outputs a sequence of frames for each token, while the rotations for atom tokens are
 264 dropped and replaced with the atom frame demonstrated in Section 4.2. The final output represents
 265 the full complex structure $\hat{\mathbf{x}}$, while token positions $\hat{\mathbf{x}}_1$ are calculated as previously described.
 266

267 **Auxiliary Head.** We add an auxiliary head to predict the pairwise binned distance from the denoised
 268 pair representation z' , $h_i = \text{softmax}(\text{Linear}(z'_i))$, which directly supervises the input of structure
 269 module and has been proved to be helpful during training (Jumper et al., 2021). The bins are also
 270 unevenly divided to accommodate the multi-scale characteristics of the predicted complex.

²Though $\hat{\mathbf{x}}_1$ is a function of $\mathbf{x}, t, f^{\text{token}}, f^{\text{feat}}$, we omitted certain parameters to simplify the text.

³To accommodate the precision differences between ligands and proteins, the bin intervals are dense between 1Å (approximate length of a chemical bond) and 3.25Å (approximate distance between adjacent amino acids) and sparser beyond 3.25Å.

270 4.4 TRAINING AND INFERENCE
271

272 We train the network $\hat{\mathbf{x}}_1$ by sampling data points and timestamps, calculating the noisy input, and
273 supervising the predicted results. At inference time, we transform the token positions sampled from
274 the prior distribution through the predicted vector field with an ODE solver, and output the structure
275 obtained at the final step.

276 **Training.** We sample the timestamp t from the logit normal distribution, assigning more weight on
277 intermediate steps, which helps the model to achieve better performance on hard timestamps (Esser
278 et al., 2024; Karras et al., 2022). The prior distribution $q(x)$ is selected as $\mathcal{N}(0, \sigma_{\text{data}})$, where
279 $\sigma_{\text{data}} = 10$. The input \mathbf{x} is given by interpolating the data point and a sample from the prior
280 distribution. The training procedure is shown in Algorithm 1.

281 **Inference.** A scheduler of noise levels $\{t_i\}_{i=0}^m, t_0 = 0, t_m = 1$ is used to determine the noise level
282 t_i of each sampling step x_{t_i} . Starting from a noisy sample $x_{t_0} = x_0$ as the initial model input, the
283 structure prediction network predicts the vector field, which gives $x_{t_{i+1}}$ with the Euler’s Method, i.e.

$$284 \mathbf{x}_{t_{i+1}} = \mathbf{x}_{t_i} + \frac{t_{i+1} - t_i}{1 - t_i} \left(\text{align}_{\mathbf{x}_{t_i}} \left(\text{Extract}(\hat{\mathbf{x}}_1(\mathbf{x}_{t_i}, t_i; \theta)) \right) - \mathbf{x}_{t_i} \right), \quad (8)$$

285 where the Extract function extracts the token positions from the predicted token frames. The model
286 output at the last step is adopted as the final result. The inference procedure is shown in Algorithm 2.

287 **Algorithm 1** Training
288

289 **Require:** data distribution $p(\mathbf{x})$, prior distribution $q(\mathbf{x})$, trainable model parameters θ
290
1: **while** not converged **do**
2: sample complex structure \mathbf{x}_1 and its corresponding ligand chemical graph \mathcal{G} from $p(\mathbf{x})$, $t \sim [0, 1]$, $\mathbf{x}_0 \sim q(\mathbf{x})$
3: $N, f^{\text{token}}, f^{\text{pair}} \leftarrow \text{Embedder}(\mathcal{G}, N_p)$
4: $\mathbf{x}_t \leftarrow t \cdot \mathbf{x}_1 + (1 - t) \cdot \text{align}_{\mathbf{x}}(\mathbf{x}_0)$
5: $\theta \leftarrow \text{Optimizer}(\theta, (\mathbf{x}_t, f^{\text{token}}, f^{\text{pair}}, t), \mathcal{L})$
6: **end while**
7: **return** θ

301 5 EXPERIMENTS
302

303 Following previous protein design models (Yim et al., 2023a; Lin & AlQuraishi, 2023; Watson
304 et al., 2023) and binder design models (Krishna et al., 2024), we evaluate ATOMFLOW through in
305 silico experiments on key metrics of our generated binder including self-consistency, binding affinity,
306 diversity and novelty.

307 5.1 EXPERIMENT SETUP
308

309 **Training Data.** We train the denoising model on two datasets: PDBBind (Liu et al., 2017), a protein-
310 ligand conformer dataset derived from the Protein Data Bank (PDB) (Berman et al., 2000), and
311 SCOPe (Chandonia et al., 2022), a structure categorical dataset for protein. The model is first trained
312 on solely generating the protein structure for 400k steps, and then finetuned on co-generating both
313 the protein and ligand structure for 300k steps.

314 **Baseline and Model Variant.** We compare ATOMFLOW with the state-of-the-art binder generation
315 method RFDiffusionAA (Krishna et al., 2024), which is extensively trained on almost all known
316 data. Since RFDiffusionAA requires a fixed ligand structure at the binding state as input, we extend
317 our method to work under its setting. For ATOMFLOW, besides the original setting (ATOMFLOW-
318 N), we also train a version of our model with the pairwise distance matrix of the bound structure
319 as an auxiliary hint input (ATOMFLOW-H). We also compare with a repurposed version of an
320 AlphaFold 3 replication model Chai-1 (team et al., 2024) (see Appendix A.5 for details).⁴ We exclude
321 PocketGen (Zhang et al., 2024) and FlowSite (Stark et al., 2024) since they can only refine the pocket
322 residues of a given binder. We discuss them with an additional experiment in the appendix.

323 ⁴Due to license restrictions, we cannot use the original AlphaFold 3. In our preliminary experiments
324 comparing Chai-1, Boltz (Wohlwend et al., 2024), and Protenix (Team et al., 2025), Chai-1 performed best and
325 is used as a substitute in this work.

Evaluation Set. Following RFDiffusionAA, we evaluate all methods on the ligand set (evaluation set) from RFDiffusionAA (CCD code⁵: FAD, SAM, IAI, OQQ). IAI and OQQ are two ligands newly added to PDB, out of the training set of all methods. We conduct an *extended evaluation* on a larger set of 20 ligands (Appendix A.6). The extended evaluation set comprises ligands from inside and outside the training set, with both long and short lengths, and the trends remain consistent with those in the main text. We also include a speed test demonstrating ATOMFLOW is 5 times faster than RFDiffusionAA in Appendix A.6.

5.2 SELF-CONSISTENCY AND CONFORMER LEGITIMACY

In this section, we evaluate the generated protein structure by self-consistency RMSD and the predicted ligand structure at the binding state by detecting structural violence in the conformer. We further evaluate the legitimacy of designed complex conformer on geometric distribution and chemical validity.

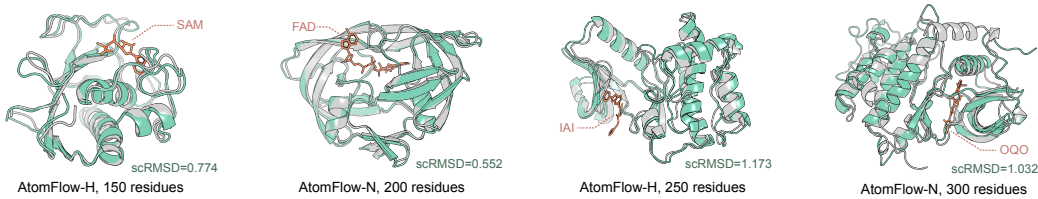


Figure 3: Designed structures for different ligands at different lengths. We align the ESMFold predicted structure to the designed structure, and report the scRMSD metric. Green: designed protein; Orange: designed ligand conformer; Grey: ESMFold predicted protein.

Protein Structure. For protein structures, self-consistency RMSD is widely adopted as a metric to evaluate their legitimacy (Lin & AlQuraishi, 2023; Watson et al., 2023), which compares the generated structure and the folding of its sequence predicted by an accurate model. We adopt LigandMPNN (Dauparas et al., 2023) to predict possible sequences from the generated structures. We first generate 8 sequences for all designed structures with LigandMPNN, then predict the corresponding protein structure with ESMFold (Lin et al., 2023), and the metric for each generated structure is calculated as the minimum rooted mean squared distance between the designed structure and predicted structure (scRMSD). For each ligand in the evaluation set, we generate 10 structures for lengths in [100, 150, 200, 250, 300]. The results are shown in Table 2. We illustrate several generated samples in Figure 3, and the cumulative distribution of scRMSD among them in Figure 4 and Figure S2B.

Method	Overall	SAM	FAD	IAI	OQQ
ATOMFLOW-H	0.57	0.60	0.36	0.58	0.74
ATOMFLOW-N	0.50	0.50	0.38	0.58	0.54
RFDiffusionAA	0.52	0.60	0.58	0.48	0.42
Chai-1	0.46	0.48	0.52	0.52	0.32
RFDiffusion	0.33	0.04	0.50	0.44	0.32

Table 2: Proportion of samples with scRMSD < 2 on the evaluation set (higher is better).

ATOMFLOW-H achieves the best overall performance on the evaluation set, ranking first on 3 out of 4 ligands. ATOMFLOW-N, the version without structural hints, also performs comparably to RFDiffusionAA, and even outperforms it on the out-of-distribution test cases IAI and OQQ. Although not specifically designed for de novo generation, Chai-1 shows acceptable performance on protein structure tasks. The relatively limited performance of RFDiffusion is expected, as its strong binding potential for guiding protein-ligand interactions can lead to structural disruption. Including structural hints from the ligand conformer slightly improves binder quality, likely because the pocket shape is partially revealed through the input.

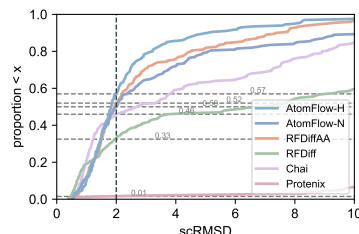


Figure 4: scRMSD distribution of samples on the evaluation set.

⁵The identifying three-letter code in the chemical components directory (Westbrook et al., 2015).

378 **Conformer Legitimacy.** We evaluate the chemical validity of the protein-ligand complex conformers
 379 with PoseBusters (Buttenschoen et al., 2024) and PoseCheck (Harris et al., 2023). We also evaluate the
 380 geometric distribution of common chemical bond lengths generated by ATOMFLOW in comparison
 381 to the ground truth bond lengths in our training set, as well as comparing the Ramachandran plots
 382 between ATOMFLOW-generated proteins and natural ones. We illustrate the results in Appendix A.6.
 383 The results indicate that ATOMFLOW generates legitimate samples with metrics close to those of the
 384 natural proteins.

385 5.3 BINDING AFFINITY

387 In this section, we evaluate binding affinity using two *in silico* metrics, acknowledging that such
 388 computational estimates can only serve as proxies. Ultimately, wet-lab experiments remain the
 389 gold standard for validating binding affinity, though they are typically too costly for large-scale
 390 benchmarking.

391 We first report the **AutoDock Vina score** (Eberhardt et al., 2021),
 392 a widely adopted docking-based energy metric (Zhang et al., 2024). For each designed binder,
 393 we pack side chains using the Rosetta packer (Leaver-Fay et al., 2011), and report the minimum docking
 394 score across all generated conformations. This score serves as an
 395 approximate measure of interaction energy between the ligand and
 396 the designed protein.

398 As a complementary signal, we compute the **min PAE interaction (min_ipAE)**—a metric derived from the Predicted Aligned
 399 Error (PAE) matrix of an AlphaFold 3-like model. Specifically,
 400 min_ipAE reflects the model’s confidence in the relative positioning between ligand and protein
 401 residues; lower values indicate higher structural confidence in the binding interface. Although originally
 402 introduced for protein–protein interactions (Zambaldi et al., 2024), this metric has demonstrated
 403 strong correlation with binder quality. To obtain min_ipAE, we input LigandMPNN-designed se-
 404 quences and their respective ligands into Chai-1 (team et al., 2024), and extract the lowest interaction
 405 PAE value between protein and ligand tokens, following the AlphaProteo protocol.

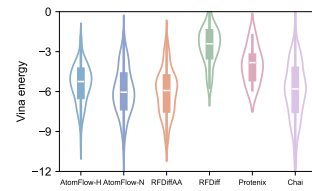


Figure 5: Vina score distribution on the evaluation set.

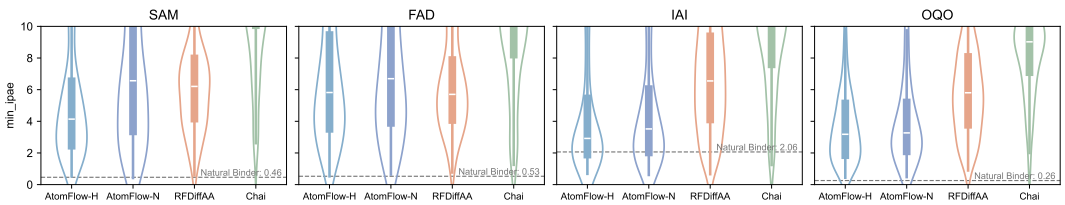
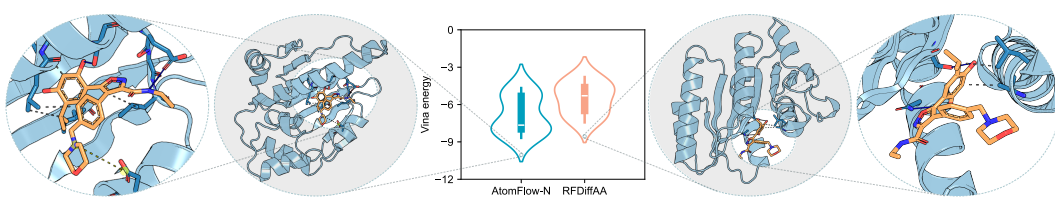


Figure 6: min PAE interaction (min_ipAE) of samples on the evaluation set (lower is better) predicted by Chai-1. The value of natural binder in PDB is highlighted.

416 As shown in Figure 6, binders generated by ATOMFLOW-H achieve lower min_ipAE than those
 417 from RFDiffusionAA on 3 of 4 ligands. ATOMFLOW-N performs slightly worse than ATOMFLOW-
 418 H but still shows strong results, without structural hint. Both ATOMFLOW and RFDiffusionAA
 419 produce results comparable to natural complexes. The AutoDock Vina results, shown in Figure 5
 420 and detailed in Figure S2A, indicates that ATOMFLOW also matches or exceeds the performance of
 421 RFDiffusionAA in terms of docking energy, aligning with the trends observed in the min_ipAE
 422 metric. Similar results are observed on the extended evaluation set (Figure S2C,D).

423 We further compare ATOMFLOW with RFDiffusionAA in a realistic setting where the bound con-
 424 former is unknown. We set the target ligand as luminespib (PDB id: 2GJ), an Hsp90 inhibitor (Pi-
 425 otrowska et al., 2018). A designed protein binder for luminespib may act as a protein drug carrier to
 426 enhance drug efficacy. Luminespib is a molecule ligand with 33 heavy atoms, so that the conformer
 427 is quite flexible when docked to different receptors. We design 10 binders for luminespib using
 428 ATOMFLOW and RFDiffusionAA. The ideal conformer from PDB is provided to RFDiffusionAA,
 429 while no conformer is provided to ATOMFLOW. The binding energy of the designed structures and
 430 one designed sample with PLIP (Adasme et al., 2021) to demonstrate the protein-ligand interaction
 431 are illustrated in Figure 7. It is shown that ATOMFLOW generates more binders with higher binding
 affinity than RFDiffusionAA, and significantly outperforms RFDiffusionAA on the lowest energy

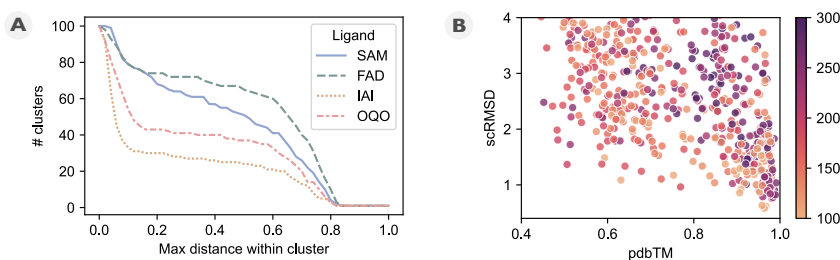


440 Figure 7: ATOMFLOW-N designs binders with lower vina energy distribution than RFDiffusionAA on
441 2GJ without the bound structure. Illustrations of one sample for each method with PLIP demonstrates
442 that the ATOMFLOW-N designed binder has more chemical interactions with the ligand.

443 among all generated structures. This demonstrates that a proper bound structure is crucial to the
444 performance of RFDiffusionAA, while ATOMFLOW does not rely on such structure and generates
445 proper conformers by co-modeling the structure space of proteins and ligands.

447 5.4 DIVERSITY AND NOVELTY

449 In this section, we report the diversity and novelty of ATOMFLOW, following common practice in
450 literature (Krishna et al., 2024; Yim et al., 2023b). Diversity refers to the structural divergence of the
451 designed binders for a certain ligand, while novelty refers to how close a designed protein is to the
452 known proteins. For diversity, we generate 100 structures with 200 residues for each ligand, and then
453 use MaxCluster (Herbert, 2008) to calculate the pairwise structural distance (TMscore) of the outputs
454 and report the number of clusters using different thresholds of the maximum distance within a cluster.
455 For novelty, we generate 4 structures with residue count in $[100, 101, \dots, 300]$ for each ligand, and
456 then calculate the highest TM-score (Zhang, 2005) between a designed structure and any similar
457 structure searched by FoldSeek (Kempen et al., 2024) (pdbTM), as well as the protein scRMSD.
458 The search range of pdbTM is all known protein structures in PDB. Results of RFDiffusionAA are
459 provided in Figure S6 (Appendix A.6).



469 Figure 8: **A:** Cluster count based on different thresholds of the maximum difference (TMscore)
470 within the cluster for each ligand in the evaluation set. ATOMFLOW generates diverse binder folds for
471 all ligands, not restricted to the existing binder structure. **B:** Scatter plot of designability (scRMSD) vs.
472 novelty (pdbTM) for ligands in the evaluation set. ATOMFLOW successfully designs self-consistent
473 structures with high pdbTM, demonstrating high novelty.

474 Figure 8A shows that ATOMFLOW produces diverse structures across ligands, with variability
475 depending on the ligand. Incorporating protein-only data during training helps the model capture
476 structural patterns beyond known complexes. As shown in Figure 8B, most generated designable
477 folds remain close to known ones, and the degree of novelty is lower than RFDiffusionAA, likely
478 due to smaller training scale, consistent with previous reports (Huguet et al.).

479 6 CONCLUSION AND FUTURE WORK

481 We propose ATOMFLOW, a de novo protein binder design method for small molecule ligands that ex-
482 plicitly models ligand flexibility without requiring a fixed conformer. By representing protein-ligand
483 complexes as unified biotokens and applying an SE(3)-equivariant flow matching framework, ATOM-
484 FLOW achieves comparable or superior binder design quality to RFDiffusionAA while offering faster
485 inference and robustness when the ligand binding conformation is unknown. We further introduce
an experimentally validated binding affinity metric for comprehensive evaluation. Future directions

486 include enabling finer structural control, scaling up training, and extending ATOMFLOW to broader
487 biomolecules such as DNA, RNA, and metal ions.
488
489
490
491
492
493
494
495
496
497
498
499
500
501
502
503
504
505
506
507
508
509
510
511
512
513
514
515
516
517
518
519
520
521
522
523
524
525
526
527
528
529
530
531
532
533
534
535
536
537
538
539

540 REPRODUCIBILITY STATEMENT
541

542 We include the source code of the AtomFlow model and its corresponding checkpoint with a ready-
543 to-use Gradio interface in the supplementary materials. Instructions for setting up the environment
544 and launching the web-based interface are provided as a README file. Further details on the model
545 implementation and training are available in Appendix A.4

546
547 REFERENCES
548

549 Josh Abramson, Jonas Adler, Jack Dunger, Richard Evans, Tim Green, Alexander Pritzel, Olaf
550 Ronneberger, Lindsay Willmore, Andrew J Ballard, Joshua Bambrick, et al. Accurate structure
551 prediction of biomolecular interactions with alphafold 3. *Nature*, pp. 1–3, 2024.

552 Melissa F Adasme, Katja L Linnemann, Sarah Naomi Bolz, Florian Kaiser, Sebastian Salentin,
553 V Joachim Haupt, and Michael Schroeder. Plip 2021: Expanding the scope of the protein–ligand
554 interaction profiler to dna and rna. *Nucleic acids research*, 49(W1):W530–W534, 2021.

555 Gustaf Ahdritz, Nazim Bouatta, Christina Floristean, Sachin Kadyan, Qinghui Xia, William Gerecke,
556 Timothy J O’Donnell, Daniel Berenberg, Ian Fisk, Niccolò Zanichelli, et al. Openfold: Retraining
557 alphafold2 yields new insights into its learning mechanisms and capacity for generalization. *Nature
558 Methods*, pp. 1–11, 2024.

559 Woody Ahern, Jason Yim, Doug Tischer, Saman Salike, Seth M Woodbury, Donghyo Kim, Indrek
560 Kalvet, Yakov Kipnis, Brian Coventry, Han Raut Altae-Tran, et al. Atom level enzyme active site
561 scaffolding using rfdiffusion2. *bioRxiv*, pp. 2025–04, 2025.

562 Michael S Albergo and Eric Vanden-Eijnden. Building normalizing flows with stochastic interpolants.
563 *arXiv preprint arXiv:2209.15571*, 2022.

564 Linna An, Meerit Y Said, Long Tran, Sagardip Majumder, Inna Goreshnik, Gyu Rie Lee, David
565 Juergens, Justas Dauparas, Ivan V. Anishchenko, Brian Coventry, Asim K. Bera, Alex Kang,
566 Paul M. Levine, Valentina Alvarez, Arvind Pillai, Christoffer H Norn, David Feldman, Dmitri
567 Zorine, Derrick R. Hicks, Xinting Li, Mariana Garcia Sanchez, Dionne K. Vafeados, Patrick J.
568 Salveson, Anastassia A. Vorobieva, and David Baker. De novo design of diverse small molecule
569 binders and sensors using shape complementary pseudocycles. *bioRxiv*, 2023. URL <https://api.semanticscholar.org/CorpusID:266540105>.

570 Nathaniel R. Bennett, Brian Coventry, Inna Goreshnik, Buwei Huang, Aza Allen, Dionne Vafeados,
571 Ying Po Peng, Justas Dauparas, Minkyung Baek, Lance Stewart, Frank DiMaio, Steven De Munck,
572 Savvas N. Savvides, and David Baker. Improving de novo protein binder design with deep
573 learning. *Nature Communications*, 14(1):2625, May 2023. ISSN 2041-1723. doi: 10.1038/s41467-023-38328-5.

574 Helen M. Berman, John D. Westbrook, Zukang Feng, Gary Gilliland, T. N. Bhat, Helge Weissig,
575 Ilya N. Shindyalov, and Philip E. Bourne. The Protein Data Bank. *Nucleic Acids Research*, 28(1):
576 235–242, 2000.

577 Matthew J Bick, Per J Greisen, Kevin J Morey, Mauricio S Antunes, David La, Banumathi Sankaran,
578 Luc Reymond, Kai Johnsson, June I Medford, and David Baker. Computational design of
579 environmental sensors for the potent opioid fentanyl. *Elife*, 6:e28909, 2017.

580 Patrick Bryant, Atharva Kelkar, Andrea Guljas, Cecilia Clementi, and Frank Noé. Structure prediction
581 of protein–ligand complexes from sequence information with umol. *Nature Communications*, 15
582 (1):4536, 2024.

583 Martin Buttenschoen, Garrett M Morris, and Charlotte M Deane. Posebusters: Ai-based docking
584 methods fail to generate physically valid poses or generalise to novel sequences. *Chemical Science*,
585 15(9):3130–3139, 2024.

586 John-Marc Chandonia, Lindsey Guan, Shiangyi Lin, Changhua Yu, Naomi K Fox, and Steven E
587 Brenner. Scope: improvements to the structural classification of proteins – extended database to
588 facilitate variant interpretation and machine learning. *Nucleic Acids Research*, 50(D1):D553–D559,
589 2022.

594 Ricky TQ Chen and Yaron Lipman. Flow matching on general geometries. In *The Twelfth International Conference on Learning Representations*, 2024.

595

596

597 Justas Dauparas, Gyu Rie Lee, Robert Pecoraro, Linna An, Ivan Anishchenko, Cameron Glasscock,

598 and David Baker. Atomic context-conditioned protein sequence design using ligandmpnn. *Biorxiv*,

599 pp. 2023–12, 2023.

600 Willem Diepeveen, Carlos Esteve-Yagüe, Jan Lellmann, Ozan Öktem, and Carola-Bibiane Schönlieb.

601 Riemannian geometry for efficient analysis of protein dynamics data. *Proceedings of the National*

602 *Academy of Sciences*, 121(33):e2318951121, 2024.

603

604 Jerome Eberhardt, Diogo Santos-Martins, Andreas F. Tillack, and Stefano Forli. Autodock Vina

605 1.2.0: New Docking Methods, Expanded Force Field, and Python Bindings. *Journal of Chemical*

606 *Information and Modeling*, 61(8):3891–3898, 2021.

607 Patrick Esser, Sumith Kulal, Andreas Blattmann, Rahim Entezari, Jonas Müller, Harry Saini, Yam

608 Levi, Dominik Lorenz, Axel Sauer, Frederic Boesel, Dustin Podell, Tim Dockhorn, Zion English,

609 and Robin Rombach. Scaling Rectified Flow Transformers for High-Resolution Image Synthesis.

610 In *Forty-first International Conference on Machine Learning*, volume abs/2403.03206, 2024.

611

612 Charles Harris, Kieran Didi, Arian R Jamasb, Chaitanya K Joshi, Simon V Mathis, Pietro Lio, and

613 Tom Blundell. Benchmarking generated poses: How rational is structure-based drug design with

614 generative models? *arXiv preprint arXiv:2308.07413*, 2023.

615 Alex Herbert. Maxcluster: A tool for protein structure comparison and clustering, 2008. URL

616 <http://www.sbg.bio.ic.ac.uk/~maxcluster/>.

617

618 Guillaume Huguet, James Vuckovic, Kilian Fatras, Eric Thibodeau-Laufer, Pablo Lemos, Ri-

619 ashat Islam, Cheng-Hao Liu, Jarrid Rector-Brooks, Tara Akhoun-Sadegh, Michael Bronstein,

620 et al. Flow matching for conditional protein backbone generation, may 2024. URL <http://arxiv.org/abs/2405.20313>.

621

622 John B Ingraham, Max Baranov, Zak Costello, Karl W Barber, Wujie Wang, Ahmed Ismail, Vincent

623 Frappier, Dana M Lord, Christopher Ng-Thow-Hing, Erik R Van Vlack, et al. Illuminating protein

624 space with a programmable generative model. *Nature*, 623(7989):1070–1078, 2023.

625

626 Dick Jardine. Euler’s method in euler’s words. *Mathematical Time Capsules: Historical Modules for*

627 *the Mathematics Classroom*, (77):215, 2011.

628

629 Bowen Jing, Bonnie Berger, and Tommi Jaakkola. Alphafold meets flow matching for generating

630 protein ensembles. *arXiv preprint arXiv:2402.04845*, 2024.

631

632 John Jumper, Richard Evans, Alexander Pritzel, Tim Green, Michael Figurnov, Olaf Ronneberger,

633 Kathryn Tunyasuvunakool, Russ Bates, Augustin Žídek, Anna Potapenko, et al. Highly accurate

634 protein structure prediction with alphafold. *nature*, 596(7873):583–589, 2021.

635

636 Tero Karras, Miika Aittala, Timo Aila, and Samuli Laine. Elucidating the design space of diffusion-

637 based generative models. *Advances in neural information processing systems*, 35:26565–26577,

638 2022.

639

640 Michel van Kempen, Stephanie S. Kim, Charlotte Tumescheit, Milot Mirdita, Jeongjae Lee, Cameron

641 L. M. Gilchrist, Johannes Söding, and Martin Steinegger. Fast and accurate protein structure search

642 with Foldseek. *Nature Biotechnology*, 42(2):243–246, 2024.

643

644 Diederik P Kingma. Adam: A method for stochastic optimization. *arXiv preprint arXiv:1412.6980*,

645 2014.

646

647 Xiangzhe Kong, Wenbing Huang, and Yang Liu. End-to-end full-atom antibody design. *arXiv*

648 *preprint arXiv:2302.00203*, 2023.

649

650 Rohith Krishna, Jue Wang, Woody Ahern, Pascal Sturmels, Preetham Venkatesh, Indrek Kalvet,

651 Gyu Rie Lee, Felix S Morey-Burrows, Ivan Anishchenko, Ian R Humphreys, et al. Generalized

652 biomolecular modeling and design with rosettafold all-atom. *Science*, 384(6693):eadl2528, 2024.

648 Andrew Leaver-Fay, Michael Tyka, Steven M Lewis, Oliver F Lange, James Thompson, Ron Jacak,
 649 Kristian W Kaufman, P Douglas Renfrew, Colin A Smith, Will Sheffler, et al. Rosetta3: an
 650 object-oriented software suite for the simulation and design of macromolecules. In *Methods in*
 651 *enzymology*, volume 487, pp. 545–574. Elsevier, 2011.

652
 653 Yeqing Lin and Mohammed AlQuraishi. Generating novel, designable, and diverse protein structures
 654 by equivariantly diffusing oriented residue clouds. *arXiv preprint arXiv:2301.12485*, 2023.

655 Zeming Lin, Halil Akin, Roshan Rao, Brian Hie, Zhongkai Zhu, Wenting Lu, Nikita Smetanin,
 656 Robert Verkuil, Ori Kabeli, Yaniv Shmueli, et al. Evolutionary-scale prediction of atomic-level
 657 protein structure with a language model. *Science*, 379(6637):1123–1130, 2023.

658
 659 Yaron Lipman, Ricky TQ Chen, Heli Ben-Hamu, Maximilian Nickel, and Matt Le. Flow matching
 660 for generative modeling. *arXiv preprint arXiv:2210.02747*, 2022.

661 Xingchao Liu, Chengyue Gong, and Qiang Liu. Flow straight and fast: Learning to generate and
 662 transfer data with rectified flow. *arXiv preprint arXiv:2209.03003*, 2022.

663
 664 Zhihai Liu, Minyi Su, Li Han, Jie Liu, Qifan Yang, Yan Li, and Renxiao Wang. Forging the Basis for
 665 Developing Protein–Ligand Interaction Scoring Functions. *Accounts of Chemical Research*, 50(2):
 666 302–309, 2017.

667 Lei Lu, Xuxu Gou, Sophia K Tan, Samuel I Mann, Hyunjun Yang, Xiaofang Zhong, Dimitrios
 668 Gazgalis, Jesús Valdiviezo, Hyunil Jo, Yibing Wu, et al. De novo design of drug-binding proteins
 669 with predictable binding energy and specificity. *Science*, 384(6691):106–112, 2024.

670
 671 David L Mobley and Ken A Dill. Binding of small-molecule ligands to proteins: “what you see” is
 672 not always “what you get”. *Structure*, 17(4):489–498, 2009.

673 Z Piotrowska, DB Costa, GR Oxnard, M Huberman, JF Gainor, IT Lennes, A Muzikansky, AT Shaw,
 674 CG Azzoli, RS Heist, et al. Activity of the hsp90 inhibitor luminespib among non-small-cell lung
 675 cancers harboring egfr exon 20 insertions. *Annals of Oncology*, 29(10):2092–2097, 2018.

676
 677 Nicholas F Polizzi and William F DeGrado. A defined structural unit enables de novo design of
 678 small-molecule–binding proteins. *Science*, 369(6508):1227–1233, 2020.

679
 680 Nadine Schneider, Roger A Sayle, and Gregory A Landrum. Get your atoms in order—an open-source
 681 implementation of a novel and robust molecular canonicalization algorithm. *Journal of chemical*
 682 *information and modeling*, 55(10):2111–2120, 2015.

683 Bettina Schreier, Christian Stumpp, Silke Wiesner, and Birte Höcker. Computational design of ligand
 684 binding is not a solved problem. *Proceedings of the National Academy of Sciences*, 106(44):
 685 18491–18496, November 2009. ISSN 0027-8424, 1091-6490. doi: 10.1073/pnas.0907950106.

686
 687 Peter Shaw, Jakob Uszkoreit, and Ashish Vaswani. Self-Attention with Relative Position Representa-
 688 tions. In *North American Chapter of the Association for Computational Linguistics (NAACL)*, pp.
 689 464–468, 2018.

690 Chence Shi, Chuanrui Wang, Jiarui Lu, Boztao Zhong, and Jian Tang. Protein sequence and structure
 691 co-design with equivariant translation. *arXiv preprint arXiv:2210.08761*, 2022.

692
 693 Yang Song, Jascha Sohl-Dickstein, Diederik P. Kingma, Abhishek Kumar, Stefano Ermon, and Ben
 694 Poole. Score-Based Generative Modeling through Stochastic Differential Equations. *International*
 695 *Conference on Learning Representations (ICLR)*, 2021.

696 Hannes Stark, Bowen Jing, Regina Barzilay, and Tommi Jaakkola. Harmonic Self-Conditioned Flow
 697 Matching for joint Multi-Ligand Docking and Binding Site Design. In *Forty-first International*
 698 *Conference on Machine Learning*, volume abs/2310.05764, 2024.

699
 700 ByteDance AML AI4Science Team, Xinshi Chen, Yuxuan Zhang, Chan Lu, Wenzhi Ma, Jiaqi
 701 Guan, Chengyue Gong, Jincai Yang, Hanyu Zhang, Ke Zhang, et al. Protenix-advancing structure
 prediction through a comprehensive alphafold3 reproduction. *bioRxiv*, pp. 2025–01, 2025.

702 Chai Discovery team, Jacques Boitraud, Jack Dent, Matthew McPartlon, Joshua Meier, Vinicius
 703 Reis, Alex Rogozhonikov, and Kevin Wu. Chai-1: Decoding the molecular interactions of life.
 704 *BioRxiv*, pp. 2024–10, 2024.

705 Joseph L. Watson, David Juergens, Nathaniel R. Bennett, Brian L. Trippe, Jason Yim, Helen E.
 706 Eisenach, Woody Ahern, Andrew J. Borst, Robert J. Ragotte, Lukas F. Milles, Basile I. M.
 707 Wicky, Nikita Hanikel, Samuel J. Pellock, Alexis Courbet, William Sheffler, Jue Wang, Preetham
 708 Venkatesh, Isaac Sappington, Susana Vázquez Torres, Anna Lauko, Valentin De Bortoli, Emile
 709 Mathieu, Sergey Ovchinnikov, Regina Barzilay, Tommi S. Jaakkola, Frank DiMaio, Minkyung
 710 Baek, and David Baker. De novo design of protein structure and function with RFdiffusion. *Nature*,
 711 620(7976):1089–1100, 2023.

712 John D Westbrook, Chenghua Shao, Zukang Feng, Marina Zhuravleva, Sameer Velankar, and Jasmine
 713 Young. The chemical component dictionary: complete descriptions of constituent molecules in
 714 experimentally determined 3d macromolecules in the protein data bank. *Bioinformatics*, 31(8):
 715 1274–1278, 2015.

716 Jeremy Wohlwend, Gabriele Corso, Saro Passaro, Mateo Reveiz, Ken Leidal, Wojtek Swiderski, Tally
 717 Portnoi, Itamar Chinn, Jacob Silterra, Tommi Jaakkola, et al. Boltz-1: Democratizing biomolecular
 718 interaction modeling. *bioRxiv*, pp. 2024–11, 2024.

719 Kevin E Wu, Kevin K Yang, Rianne van den Berg, Sarah Alamdar, James Y Zou, Alex X Lu, and
 720 Ava P Amini. Protein structure generation via folding diffusion. *Nature communications*, 15(1):
 721 1059, 2024.

722 Nianzu Yang, Jian Ma, Songlin Jiang, Huaijin Wu, Shuangjia Zheng, Wengong Jin, and Junchi Yan.
 723 Repurposing alphafold3-like protein folding models for antibody sequence and structure co-design.
 724 In *ICLR 2025 Workshop on Generative and Experimental Perspectives for Biomolecular Design*.

725 Jason Yim, Andrew Campbell, Andrew YK Foong, Michael Gastegger, José Jiménez-Luna, Sarah
 726 Lewis, Victor Garcia Satorras, Bastiaan S Veeling, Regina Barzilay, Tommi Jaakkola, et al. Fast
 727 protein backbone generation with se (3) flow matching. *arXiv preprint arXiv:2310.05297*, 2023a.

728 Jason Yim, Brian L Trippe, Valentin De Bortoli, Emile Mathieu, Arnaud Doucet, Regina Barzilay,
 729 and Tommi Jaakkola. Se (3) diffusion model with application to protein backbone generation.
 730 *arXiv preprint arXiv:2302.02277*, 2023b.

731 Vinicius Zambaldi, David La, Alexander E Chu, Harshnira Patani, Amy E Danson, Tristan OC Kwan,
 732 Thomas Frerix, Rosalia G Schneider, David Saxton, Ashok Thillaisundaram, et al. De novo design
 733 of high-affinity protein binders with alphaproteo. *arXiv preprint arXiv:2409.08022*, 2024.

734 Y. Zhang. Tm-align: a protein structure alignment algorithm based on the TM-score. *Nucleic Acids
 735 Research*, 33(7):2302–2309, 2005.

736 Zaixi Zhang, Wanxiang Shen, Qi Liu, and Marinka Zitnik. Pocketgen: Generating Full-Atom
 737 Ligand-Binding Protein Pockets. *bioRxiv*, 2024.

738

739

740

741

742

743

744

745

746

747

748

749

750

751

752

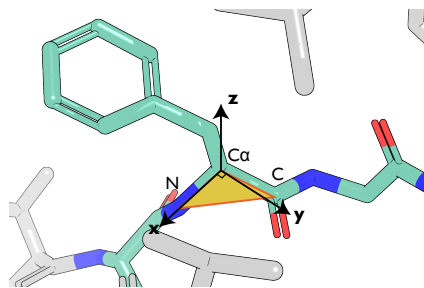
753

754

755

756 **A APPENDIX**
757758 **A.1 PROTEIN FRAMES**
759

760 Proteins are composed of amino acid chains linked by peptide bonds, forming a backbone with
761 protruding side chains. Each amino acid's position and orientation are described by a local coordinate
762 system, or protein frame, centered on three key backbone atoms: the alpha carbon ($C\alpha$), the carbonyl
763 carbon (C), and the amide nitrogen (N). These atoms act as reference points for establishing the frame.
764 The alpha carbon ($C\alpha$) typically acts as the origin. The vector from $C\alpha$ to the amide nitrogen (N) is
765 normalized to define one axis of the frame. A second axis is defined by the normalized vector from
766 $C\alpha$ to the carbonyl carbon (C). The third axis is formed by the cross product of these two vectors,
767 creating an orthogonal, right-handed coordinate system. The residue frame is typically represented
768 as an $SE(3)$ transformation $T = (R, t)$, which maps a vector from this local system to the global
769 coordinate system. In this transformation, t corresponds to the position of $C\alpha$ in the global system,
770 and R represents the rotation needed to align the residue's structure within the global context.



781 Figure S1: A protein frame illustration. The $C\alpha$, C, N atoms form a panel, which is the xy panel. The
782 x-axis is defined as the orientation from $C\alpha$ to N, while the y-axis is on the panel and perpendicular
783 to the x-axis. The z-axis is perpendicular to the xy panel.

784 **A.2 DETAILS ON BIOTOKENS**
785

786 **Token Features.** For ligand atom tokens, the token-level feature set includes: chirality, degree, formal
787 charge, implicit valence, number of H atoms, number of radical electrons, orbital hybridization,
788 aromaticity, and ring size. The pair-level feature is provided as one-hot embedding of the bond type.
789 For residue tokens, no token-level feature is known, [while the pair-level features are optional and
790 may contain the binned distance of residue index between residues for fully de novo generation \(our
791 experiment\), and motif structures can be provided as additional pairwise features when needed](#). All
792 features are encoded as a one-hot vector and concatenated.

793 **Token Frames.** The final loss we adopted $\mathcal{L}_{CFM-FAPE}$ requires aligning the predicted structure to the
794 local frame of every token. The frames of protein residues can be naturally defined as in Section 3.
795 However, the frames of ligand atoms could not be chosen directly. Since a frame could be calculated
796 from the coordinate of 3 atoms, we need to choose an atom triplet for every atom token.

797 We first obtain a canonical rank of every atom that does not depend on the input order (Schneider
798 et al., 2015). The atoms are then renamed to their rank. For atoms x with a degree greater than or
800 equal to 2, we select the lexicographically smallest triplet (u, x, v) to define the frame, where u and
801 v are neighbors of x . For atoms with a degree of 1, u is the only neighbor of x , and v is chosen as
802 one of u 's neighbors. This method ensures that each atom's frame is defined in a consistent manner,
803 irrespective of its position in the input sequence, thereby facilitating the model to learn a consistent
804 structural target.

805 **Extending Token Types and Features.** Though ATOMFLOW only considers the interaction between
806 protein and molecule ligands, the unified biotoken has the potential to extend to all biological entities,
807 including DNA, RNA, etc, by defining the token position, token frame, local and pair features, and
808 the representation of the internal structure. For example, an RNA can be represented as a sequence of
809 nucleotides, with the token position defined as its mass center, and the token frame calculated from
an atom triplet, such as C2-N1-C6.

810 The token features can also be extended to support more types of known information. For example,
 811 the local features could also contain an embedding to indicate the preferred secondary structure, or
 812 whether a ligand atom is required to be closer to the designed protein; the pair features could also
 813 contain the motif information with a distance map.

814
 815 **A.3 DETAILS ON THE FLOW MATCHING PROCESS**

816 For all types of tokens, we only consider their token positions to simplify the flow matching process.
 817 Thus, the positions of all tokens lie in the Euclidean space $\mathbb{R}^{N \times 3}$. Since a complex could be arbitrarily
 818 moved or rotated in the coordinate space without changing its structure, we need an algorithm that
 819 treats different position series as the same if they could be aligned with an SE(3) translation. Thus,
 820 every data point we consider now lies in the quotient space $\mathbb{R}^{N \times 3}/\text{SE}(3)$. This quotient space is
 821 proved to be a Riemannian manifold (Diepeveen et al., 2024).

822 For a Riemannian manifold, the flow matching process could be defined using a premetric (Chen &
 823 Lipman, 2024). A premetric $d : \mathcal{M} \times \mathcal{M} \rightarrow \mathbb{R}$ should satisfy: 1. $d(x, y) \geq 0$ for all $x, y \in \mathcal{M}$; 2.
 824 $d(x, y) = 0$ iff $x = y$; 3. $\nabla d(x, y) \neq 0$ iff $x \neq y$.

825 We define our premetric as the minimum point-wise rooted sum of squared distance (RMSD) among
 826 all pairs of possible structures in the original space $\mathbb{R}^{N \times 3}$ for two elements in the quotient space
 827 $d(x, y) = \|\text{align}_x(y) - x\|$, which satisfies all three conditions.

828
 829 *Proof.* Since the premetric is defined as a norm, it satisfies condition 1 by nature. When $x = y$, the
 830 best alignment that aligns y to x could derive the exact same position as x , yielding a zero norm.
 831 When $x \neq y$, when y is aligned to x , there's still a structural difference between the structures, thus
 832 the premetric is not zero. For condition 3, by defining $y' = \text{align}_x(y)$, we have

$$833 \nabla d(x, y) = \nabla \sqrt{\sum_{i=1}^n (y'_i - x_i)^2} = \frac{y' - x}{\|y' - x\|} = \frac{\text{align}_x(y) - x}{\|\text{align}_x(y) - x\|} \geq 0. \quad (9)$$

834 Thus $d(x, y)$ satisfies all the conditions as a qualified premetric. \square

835 With such premetric, and a monotonically decreasing differentiable scheduler $\kappa(t) = 1 - t$, we could
 836 obtain a well-defined conditional vector field that linearly interpolates between the noisy and real
 837 data (Chen & Lipman, 2024)

$$838 u_t(x|x_1) = \frac{d \log \kappa(t)}{dt} d(x, x_1) \frac{\nabla d(x, x_1)}{\|\nabla d(x, x_1)\|^2} = \frac{1}{1-t} (\text{align}_x(x_1) - x). \quad (10)$$

839 The vector field in equation 10 is calculated by substituting equation 9 into the left side. This vector
 840 field provides the direction for moving straight towards x_1 , and generates a probability flow that
 841 interpolates linearly between noisy sample x_0 and data sample x_1 .

842 Since the vector field is defined as a function of x_1 , we could learn the vector field with a structure
 843 prediction model $\hat{x}_1(x, t; \theta)$. By substituting equation 10 into equation 2, we obtain the training loss

$$844 \mathcal{L}_{\text{CFM}}(\theta) = \mathbb{E}_{t, p_{\text{data}}(x_1), p_t(x|x_1)} \left\| \frac{1}{1-t} (\text{align}_x(\hat{x}_1(x, t; \theta)) - \text{align}_x(x_1)) \right\|. \quad (11)$$

845 **Loss Function** \mathcal{L}_{CFM} calculates an aligned RMSD by aligning x_1 and \hat{x}_1 to x , while the FAPE loss
 846 calculates an averaged RMSD by aligning \hat{x}_1 to each residue frame of x_1 , which could be extended
 847 to the token frame (Appendix A.2). Let $\text{align}_{x,i}(y)$ denote aligning y to the i -th token frame of x , we

864 have

$$\begin{aligned}
 \mathcal{L}_{\text{CFM}} &= \mathbb{E}_{t, p_{\text{data}}(x_1), p_t(x|x_1)} \left\| \frac{1}{1-t} (\text{align}_x(\hat{x}_1(x, t; \theta)) - \text{align}_x(x_1)) \right\| \\
 &\approx \mathbb{E}_{t, p_{\text{data}}(x_1), p_t(x|x_1)} \left\| \frac{1}{1-t} \cdot \frac{1}{N} \sum_{i=1}^N (\text{align}_{x,i}(\hat{x}_1(x, t; \theta)) - \text{align}_{x,i}(x_1)) \right\| \\
 &\approx \mathbb{E}_{t, p_{\text{data}}(x_1), p_t(x|x_1)} \left\| \frac{1}{1-t} \cdot \frac{1}{N} \sum_{i=1}^N (\text{align}_{x_1,i}(\hat{x}_1(x, t; \theta)) - \text{align}_{x_1,i}(x_1)) \right\| \\
 &\approx \mathbb{E}_{t, p_{\text{data}}(x_1), p_t(x|x_1)} \left\| \frac{1}{1-t} \cdot \frac{1}{N} \sum_{i=1}^N (\text{align}_{x_1,i}(\hat{x}_1(x, t; \theta)) - x_1) \right\| \\
 &= \mathcal{L}_{\text{CFM-FAPE}}
 \end{aligned}$$

878 **Proposition 1.** $\text{align}_{x_1}(\hat{x}_1) = x_1 \iff \mathcal{L}_{\text{CFM}} = 0 \iff \mathcal{L}_{\text{CFM-FAPE}} = 0$.

880 *Proof.* When $\text{align}_{x_1}(\hat{x}_1) = x_1$, we have $\forall i, \text{align}_{x_1,i}(\hat{x}_1) = x_1$. As a result, $\mathcal{L}_{\text{CFM}} = \mathcal{L}_{\text{CFM-FAPE}} = 0$. This establishes that:

$$883 \text{align}_{x_1}(\hat{x}_1) = x_1 \iff \mathcal{L}_{\text{CFM}} = 0 \quad \text{and} \quad \text{align}_{x_1}(\hat{x}_1) = x_1 \iff \mathcal{L}_{\text{CFM-FAPE}} = 0. \quad (12)$$

884 Now, assume $\mathcal{L}_{\text{CFM}} = 0$. Suppose $\text{align}_{x_1}(\hat{x}_1) \neq x_1$. Then for all transformations R and t , we
885 have $R\hat{x}_1 + t \neq x_1$, which implies: $\|\text{align}_{x_1}(\hat{x}_1) - x_1\| \neq 0$, leading to $\mathcal{L}_{\text{CFM}} \neq 0$. This is a
886 contradiction. Therefore, $\text{align}_{x_1}(\hat{x}_1) = x_1$. This proves that

$$888 \mathcal{L}_{\text{CFM}} = 0 \iff \text{align}_{x_1}(\hat{x}_1) = x_1. \quad (13)$$

889 Similarly, assume $\mathcal{L}_{\text{CFM-FAPE}} = 0$. Suppose $\text{align}_{x_1}(\hat{x}_1) \neq x_1$. Then: $\|\text{align}_{x_1,i}(\hat{x}_1) - x_1\| \neq 0$,
890 which leads to $\mathcal{L}_{\text{CFM-FAPE}} \neq 0$, again a contradiction. Therefore, $\text{align}_{x_1}(\hat{x}_1) = x_1$. This proves that:

$$892 \mathcal{L}_{\text{CFM-FAPE}} = 0 \iff \text{align}_{x_1}(\hat{x}_1) = x_1. \quad (14)$$

893 The proposition is proved by combining equation 12,13,14. \square

894 This means that both \mathcal{L}_{CFM} and $\mathcal{L}_{\text{CFM-FAPE}}$ provide an optimization direction towards minimizing the
895 SE(3) invariant structural difference between the predicted structure and the ground truth structure.
896 Thus, we adopt $\mathcal{L}_{\text{CFM-FAPE}}$ as a realistic approximation of \mathcal{L}_{CFM} and adopt it as the training objective
897 during evaluation.

898 We divide the FAPE loss into protein-protein interaction, protein-ligand interaction, ligand-ligand
899 interaction, and assign different Z s for the three parts. For the auxiliary head, we adopt the cross-
900 entropy loss averaged over all token pairs for the predicted distance. The final training loss

$$903 \mathcal{L} = \alpha_1 \mathcal{L}_{\text{CFM-FAPE-pp}} + \alpha_2 \mathcal{L}_{\text{CFM-FAPE-pl}} + \alpha_3 \mathcal{L}_{\text{CFM-FAPE-li}} + \alpha_4 \mathcal{L}_{\text{aux}}. \quad (15)$$

905 A.4 DETAILS ON THE PREDICTION NETWORK

906 **Structure Module Specifications.** The main components of the structure module are derived from
907 AlphaFold 2 (Jumper et al., 2021), while our implementation builds on top of the widely acknowledged
908 reimplementations OpenFold (Ahdritz et al., 2024). The TransformerStack consists of 14 layers of
909 simplified Evoformer block, and the IPAStack consists of 4 layers of Invariant Point Attention (IPA)
910 blocks. The MSA operations in the Evoformer block are simplified by replacing the operations on
911 the MSA feature matrix with the single representation s_i . The weights of the IPA blocks are shared,
912 and the structural loss is calculated on the outputs of each block and averaged.

913 **Training Details.** During training, we equally sample data from the SCOPe dataset (v2.08) and the
914 PDBBind dataset (2020). We simply drop the data with more than 512 tokens, and we don't crop
915 the filtered complexes since the cutoff is large enough and only filters out a relatively small portion
916 of the data. We train our model on 10 NVIDIA RTX 4090 acceleration cards, with a batch size set
917 to 10, which means the batch size on each device is set to 1. We use the Adam Optimizer (Kingma,

918 2014) with a weight-decaying learning rate scheduler, starting from 10^{-3} and decays the learning
 919 rate by 0.95 every 50k steps. We separate the training process into two stages: 1) initial training,
 920 $\alpha_1 = 0.5, \alpha_4 = 0.3, \alpha_2 = \alpha_3 = 0$; 2) finetuning, $\alpha_1 = \alpha_2 = \alpha_3 = 0.5, \alpha_4 = 0.3$.

921 Ligand tokens are not given during the first training stage. The first stage trains an unconditional
 922 protein generation model, while the second stage turns it to a conditional protein binder and ligand
 923 conformer generation model. The FAPE loss is defined as an average of all pairs of tokens in the
 924 original paper, so the calculation process first yield a FAPE matrix and then produce the average
 925 value of the matrix. The protein-protein, protein-ligand and ligand-ligand loss calculates the average
 926 value of the sub-matrixs defined as (row: protein, col: protein), (row: protein, col: ligand), and (row:
 927 ligand, col:ligand).

928 Since training a protein design model is significantly time-consuming, the design choices of our
 929 training strategy are largely determined by grid searching possible design space and we save the
 930 training trajectory of the first 30~50k steps. We compare the training trajectories and select the best
 931 configuration that meets the following criteria: a) The final distogram loss should be close to the
 932 minimum we get among the configurations (around 2.0). b) The $\mathcal{L}_{\text{CFM-FAPE}}$ should not decline too
 933 fast at the first 10k steps. The first 10k steps are for the transformer stack to learn a relatively steady
 934 output, indicated by the decline of the distogram loss. A decline of $\mathcal{L}_{\text{CFM-FAPE}}$ at this stage will result
 935 in an undesired local minimum. Then $\mathcal{L}_{\text{CFM-FAPE}}$ should decline fast right after the distogram loss
 936 turns to decline much smoother. We select the configuration with the lowest $\mathcal{L}_{\text{CFM-FAPE}}$ at the end of
 937 training.

938 We decide the end of each training stage when the training converges, with the following criteria: a)
 939 the decline rate of every single loss is small. b) the structural violence of sampled structures (counts
 940 of CA atom violation) converges.

941 An initial study on directly training the second stage shows unsatisfactory training trajectory. Since
 942 the ligand conformer is way easier to generate compared to protein folds, the FAPE loss declines too
 943 fast even before the distogram loss, resulted in unstable TransformerStack output, and leading to a
 944 diverge of the model after around 30k steps. The resulted model with minimum loss is able to predict
 945 the ligand structure, with random protein residue position, which is unusable.

947 A.5 EVALUATION DETAILS

949 **Specifications.** Following RFDiffusionAA, we use FAD, SAM, IAI, and OQO as the selected
 950 evaluation set. FAD and SAM are witnessed by both models as training data, while IAI and OQO are
 951 not, demonstrating the generalization ability. To further investigate the performance of our method,
 952 we conduct experiments on an extended set of 20 ligands (ligands from PDB id 6cjs, 6e4c, 6gj6, 5zk7,
 953 6qto, 6i78, 6ggd, 6cjj, 6i67, 6iby, 6nw3, 6o5g, 6hlb, 6efk, 6gga, 6mhd, 6i8m, 6s56, 6tel, and 6ffe).
 954 The extended dataset includes ligand sizes (including hydrogen) ranging from 21 to 104 in length.

955 **Extended Set.** We illustrate the designability (scRMSD) and binding affinity (Vina energy) of
 956 ATOMFLOW-N in Figure S2. The extended evaluation shows that the performance of ATOMFLOW
 957 on the extended set is similar to the evaluation set shown in the main article, and demonstrates that
 958 ATOMFLOW is able to tackle almost all kinds of ligands.

960 **Repurposing Chai-1 for Structure Generation.** To enable protein design with Chai-1, we replace
 961 the protein sequence with N UNK tokens as a placeholder chain and use the ligand SMILES string as
 962 the second chain. This allows Chai-1 to treat the input as a protein-ligand complex and generate 3D
 963 structures accordingly. No model weights or architecture were changed; only the input formatting
 964 was adapted. Despite not being trained for design, Chai-1 can produce reasonable structures under
 965 this setup; however, the resulting protein-ligand interfaces often lack clear or meaningful binding
 966 patterns.

967 A.6 ADDITIONAL RESULTS

970 **Speed Comparasion with RFDiffusionAA.** We conducted experiments to generate samples for
 971 the ligand FAD using AtomFlow and RFAA, with amino acid lengths of 100, 150, 200, 250, and
 300. For each length, we measured the time (in minutes) required to generate a single sample. Each

972 experiment was repeated three times, and we reported the average time along with the standard error.
 973 During the experiments, each method had exclusive access to its respective GPU.
 974

	$L = 100$	$L = 150$	$L = 200$	$L = 250$	$L = 300$
AtomFlow	0.49 ± 0.0	0.51 ± 0.01	0.58 ± 0.01	0.79 ± 0.01	0.88 ± 0.0
RFAA	2.48 ± 0.03	2.75 ± 0.04	3.23 ± 0.01	4.02 ± 0.04	4.58 ± 0.05
Speedup	5.06x	5.39x	5.57x	5.09x	5.2x

980 Table 3: Comparison of AtomFlow and RFAA at different sequence lengths L
 981

982 **Extended Evaluation.** We compare AtomFlow-N and RFDiffusionAA on the extended set of 20
 983 ligands. The results are shown in Figure S2. ATOMFLOW matching or surpassing the performance of
 984 RFDiffusionAA on self-consistency RMAD, Vina energy and `min_ipAE`.

985 **Discussion on Pocket Design Models.** While the pocket design models address ligand-protein
 986 interactions, their focus is limited to refining pocket residues within a predefined radius. They lack
 987 the capacity to design full protein folds, making direct comparison with AtomFlow infeasible. We
 988 conducted an unfair experiment with PocketGen by providing a template binder to it, as detailed in
 989 Tabel 4. Despite this, the results demonstrate that AtomFlow consistently outperforms PocketGen in
 990 terms of fold quality across all radii.

991 For this experiment, we used the natural binders of four ligands—FAD (7bkc), SAM (7c7m), IAI
 992 (5sdv), and OQO (7v11)—as input. To evaluate the design capability of PocketGen (PG) under
 993 different constraints, we progressively increased the design radius (minimum distance to ligand)
 994 from 3.5 to 9.5. The masked target area expanded with the radius, requiring the model to redesign
 995 increasingly larger regions of the protein. When the radius exceeded the protein’s dimensions, all
 996 residues were masked, simulating our full-design setting. The table below presents the min/median
 997 scRMSD values for designs generated by PocketGen at each radius. For reference, scRMSD <
 998 2 is generally considered a successful design. Notably, PocketGen’s performance deteriorated
 999 significantly as the radius increased, reflecting its reliance on template residues. At radius=8 for
 1000 OQO, PocketGen generated designs with several residues misaligned with the ligand, leading to
 1001 abnormally high scRMSD values. PocketGen does not support radius settings beyond 10, preventing
 1002 direct simulation of the fully template-free design scenario. The results of ATOMFLOW are from our
 1003 main experiment.

Ligand	AtomFlow ($r=\infty$)	PG ($r=3.5$)	PG ($r=5$)	PG ($r=6.5$)	PG ($r=8$)	PG ($r=9.5$)
FAD	0.79/3.74	7.10/7.38	6.75/7.81	7.29/8.35	20.92/24.23	23.12/25.23
SAM	0.83/2.01	2.12/2.62	2.77/2.99	2.94/4.03	12.39/14.49	13.79/14.74
IAI	0.56/1.82	0.71/0.85	0.95/1.02	2.04/2.28	3.59/5.53	9.02/11.71
OQO	0.59/1.63	1.20/1.26	1.70/1.79	2.40/2.45	11.59/11.94	2.13/2.41

1004 Table 4: Comparison of AtomFlow and PocketGen (PG) on ligand-protein design tasks. For each
 1005 ligand, we report the minimum/median scRMSD (in Å) of designed structures. AtomFlow results are
 1006 shown for the full-design setting ($r = \infty$), while PocketGen results are shown for increasing design
 1007 radii ($r = 3.5$ to 9.5). Lower scRMSD indicates better structural accuracy. PocketGen performance
 1008 degrades as the design radius increases, highlighting its reliance on template residues.

1009 **Geometrical Distributions of Generated Structures.** We evaluated the common chemical bond
 1010 length generated by AtomFlow vs. the ground truth bond length in our training set. Results shown
 1011 in Figure S3 demonstrate that the AtomFlow generated ligands have similar geometric distribution
 1012 to ground truth. We further evaluated the generated structures by plotting the Ramachandran plots.
 1013 Results shown in Figure S4 suggests that the proteins generated by AtomFlow effectively capture the
 1014 key structural characteristics of natural proteins.

1015 **Chemical Validity of Generated Structures.** We use PoseBusters to evaluate the ligand conformer
 1016 quality of AtomFlow-generated structures. On the extended evaluation set, 71.8% of conformers
 1017 generated by AtomFlow-H pass all 19 tests (98.8% pass at least 18), whereas 51.4% of conformers
 1018 from AtomFlow-N pass all 19 tests (82.3% pass at least 18). Since RFDiffusion-AA takes a fixed
 1019 ligand conformer as input and outputs it without modification, so its score is entirely determined by
 1020 the input and does not reflect model behavior.

1026 We also use PoseCheck, a toolkit developed as part of a benchmark for structure-based drug design.
 1027 Results are shown in Figure S5. While our primary objective is to develop a ligand-binding protein,
 1028 instead of drug design, we find their metrics valuable for assessing the interaction and chemical
 1029 validity of the protein-ligand complex. We report the following three metrics:

1030 *Clash (lower is better)* evaluates the plausibility of protein-ligand binding poses by measuring the
 1031 number of atomic pairs within a distance smaller than their van der Waals radii.

1032 *Strain (lower is better)* assesses ligand conformational plausibility by calculating the difference in
 1033 internal energy before and after ligand relaxation.

1035 *Interactions (higher is better)* quantifies the number of chemical interactions formed in protein-ligand
 1036 complexes, focusing on four types: Hydrogen Bond Acceptors, Hydrogen Bond Donors, Van der
 1037 Waals Contacts, and Hydrophobic Interactions. Hyrophobic interactions and Van der Waals Contacts
 1038 are illustrated separately.

1039 We also report the PoseBusters results for AtomFlow-generated ligands on the extended evaluation
 1040 set: For AtomFlow-H, 71.8% pass all 19 tests; 98.8% pass ≥ 18 . For AtomFlow-N: 51.4% pass all
 1041 19 tests; 82.3% pass ≥ 18 .

1042 **Diversity and Novelty Results of the Baseline.** We conducted the diversity and novelty experiment
 1043 on RFDiffusion-AA with the same configuration as our results reported in the main text. The results
 1044 are shown in Figure S6. The diversity of AtomFlow designs is better than RFDiffusion-AA, while
 1045 the AtomFlow generated results tend to be more conservative in terms of pdbTM novelty. We believe
 1046 this is because we didn't train AtomFlow on a full training set including all PDB structures and the
 1047 distillation data. This is our future work and we'll release an updated model once available.

1049 A.7 LLM USAGE

1051 We use large language models (LLMs) for polishing writing, performing grammar checks, and
 1052 implementing various utility scripts. LLMs made no contribution to experimental data analysis or the
 1053 generation of research ideas. All outputs produced by LLMs were carefully reviewed and verified by
 1054 the authors.

1055
 1056
 1057
 1058
 1059
 1060
 1061
 1062
 1063
 1064
 1065
 1066
 1067
 1068
 1069
 1070
 1071
 1072
 1073
 1074
 1075
 1076
 1077
 1078
 1079

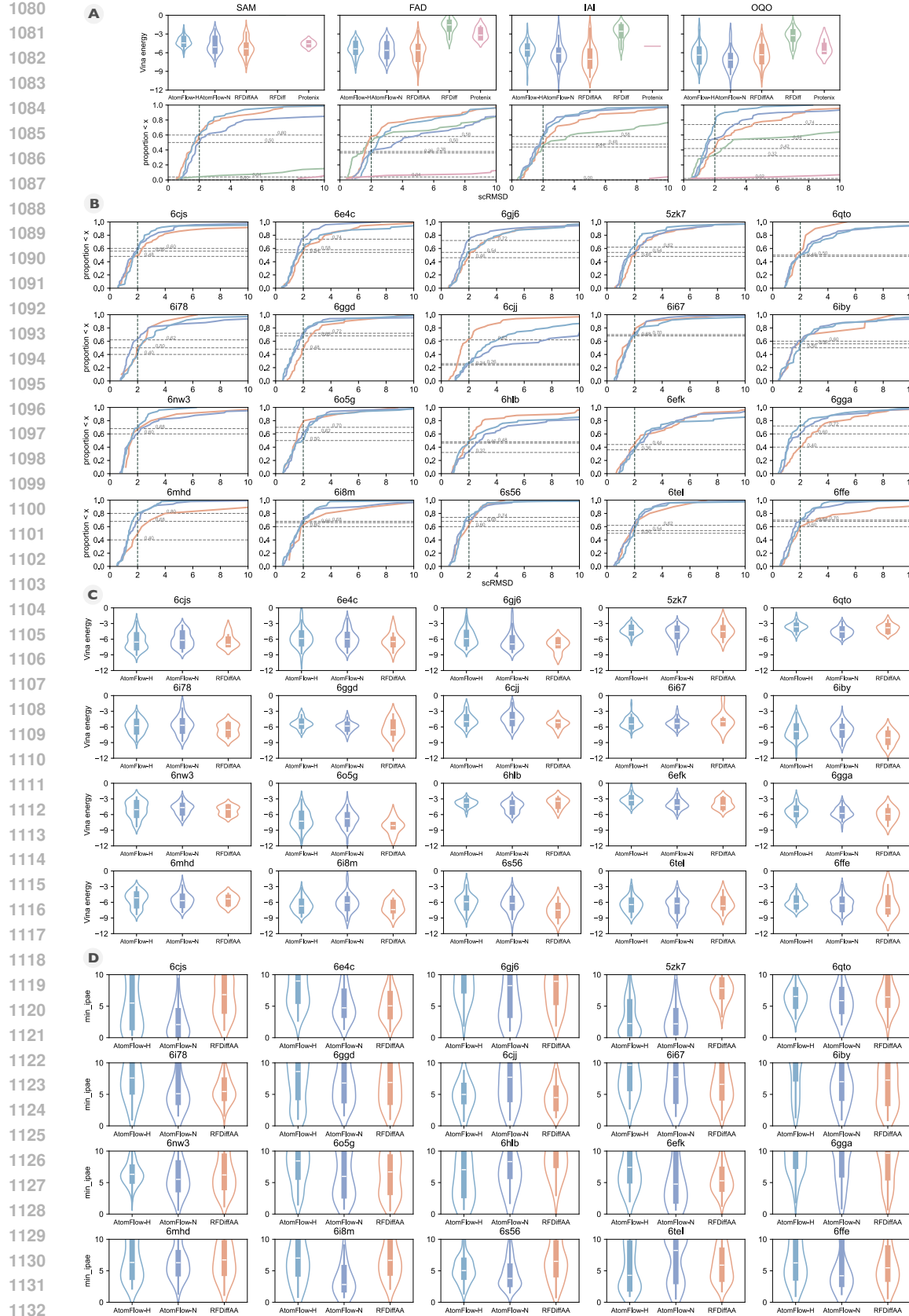


Figure S2: A: scRMSD and Vina energy of designs for the evaluation set; B: scRMSD of designs for the extended set; C: Vina energy of designs for the extended set; D: min_ipAE results for the extended set.

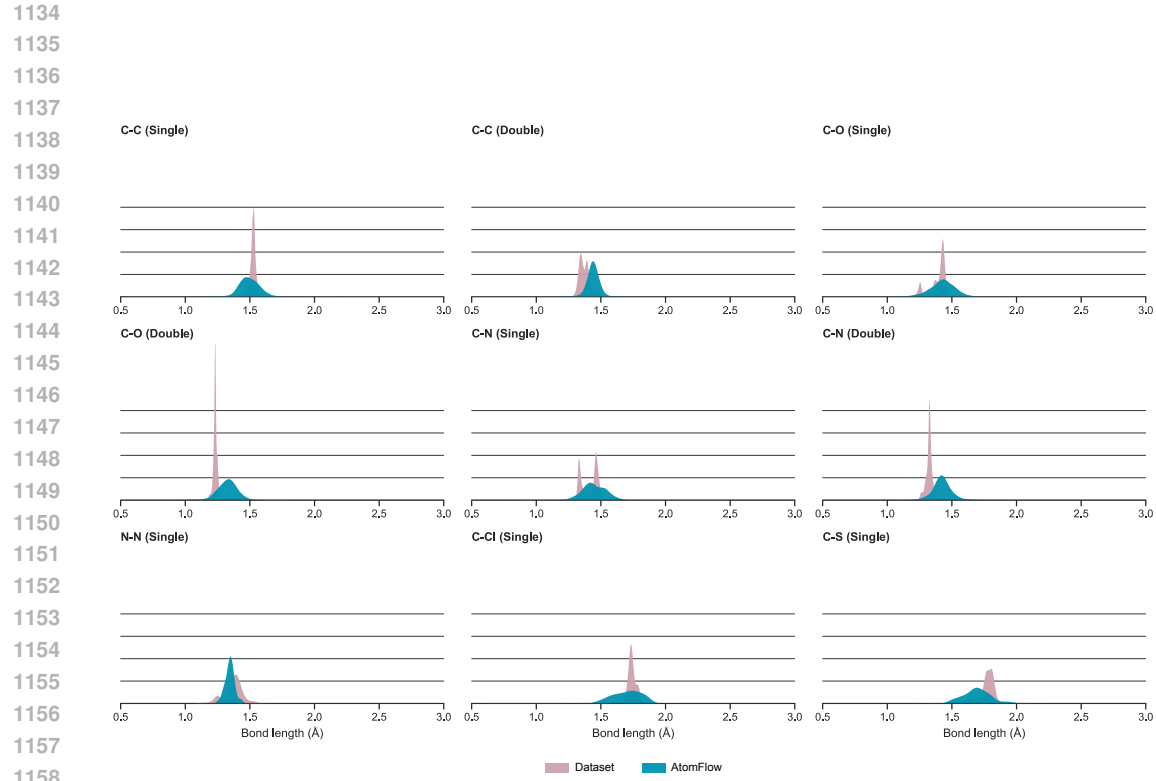


Figure S4: The Ramachandran plots for the generated protein (left) and the PDDBind protein (right), which demonstrate comparable **coverage** in the primary secondary structure regions.

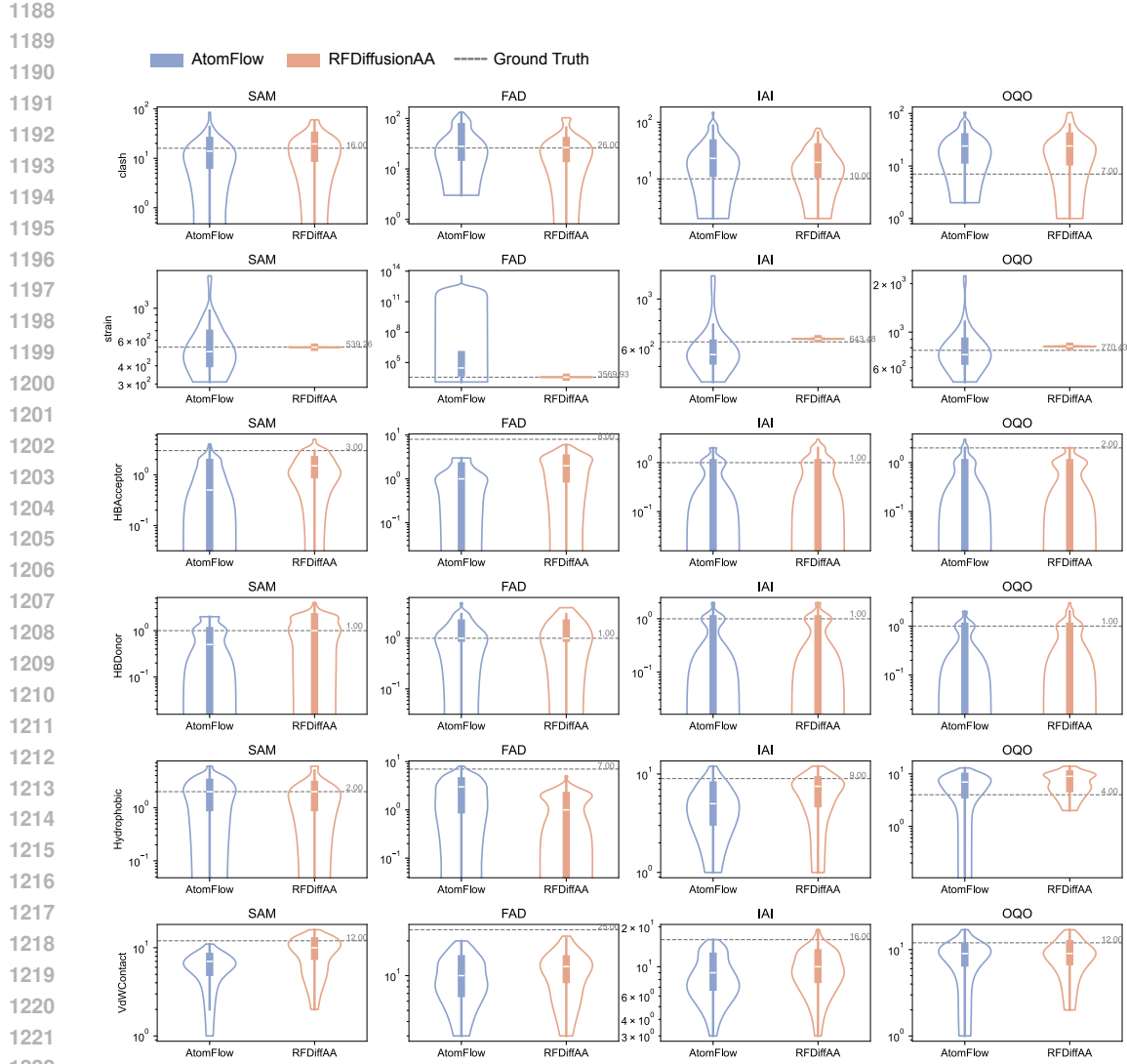


Figure S5: PoseCheck results of AtomFlow generated, RFDiffusionAA generated, and ground truth complex for the evaluation set.

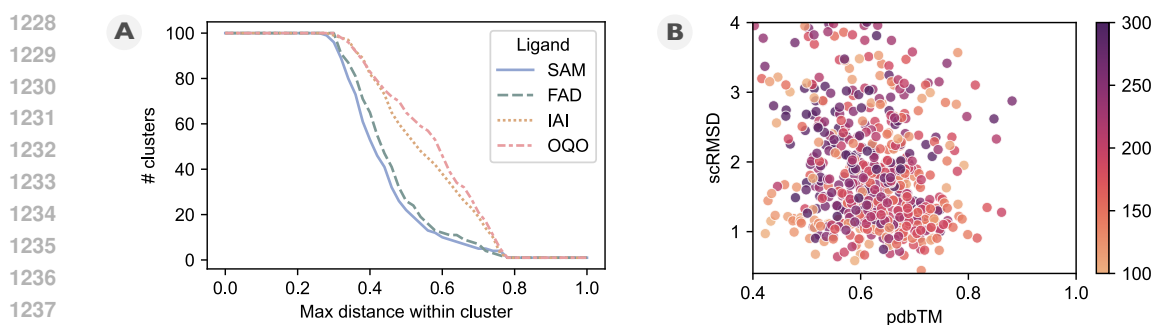


Figure S6: **A:** Cluster count based on different thresholds of the maximum difference within the cluster for each ligand in the evaluation set. **B:** Scatter plot of designability (scRMSD) vs. novelty (pdbTM) for ligands in the evaluation set.